Flux mobility delocalization in the Kitaev spin ladder

Alexandros Metavitsiadis[*] and Wolfram Brenig[†]

Institute for Theoretical Physics, Technical University Braunschweig, D-38106 Braunschweig, Germany

We study the Kitaev spin-1/2 ladder, a model which exhibits self-localization due to fractionalization caused by exchange frustration. When a weak magnetic field is applied, the model is described by an effective fermionic Hamiltonian, with an additional time-reversal symmetry-breaking term. We show that this term alone is not capable of delocalizing the system but flux mobility is a prerequisite. For magnetic fields larger but comparable to the flux gap, fluxes become mobile and drive the system into a delocalized regime, featuring finite dc transport coefficients. Our findings are based on numerical techniques, exact diagonalization, and dynamical quantum typicality, from which we present results for the specific heat, the dynamical energy current correlation function, as well as the inverse participation ratio, contrasting the spin against the fermion representation.

I. INTRODUCTION

Quantum spin liquids (QSL) are intriguing states of strongly correlated and highly entangled magnetic moments lacking spontaneous symmetry-breaking and finite local-order parameters down to zero temperature $T = 0$ K [1–3]. Instead, they feature topological order parameters and fractional excitations. One renown example of a $\mathbb{Z}_2$ QSL is the exactly solvable, two-dimensional (2D), Kitaev, spin-1/2 model (KSM), on a Honeycomb lattice [4,5]. The spins that reside on the vertices of the Honeycomb lattice exhibit frustrating compass interactions and as a result fractionalize into fermions and $\mathbb{Z}_2$ gauge fluxes. Hence the total Hilbert space is fragmented in subspaces with reduced or absent translation symmetry. While the ground state resides in a uniform flux sector, fluxes can be thermally excited, thus becoming a temperature-activated binary disorder for the fermions to scatter off.

Besides the original 2D-KSM, variants of it with different spin [6–8] or dimensionality have also been discussed in the literature [9–16]. The Kitaev ladder, a 1D KSM, is a very interesting model because the reduced dimensionality inflicts additional peculiarities on it. The fermionic representation with the emergent $\mathbb{Z}_2$ gauge field still holds, but in 1D the scattering off of fermions on disorder leads to localization [13]. Thus in the 1D-KSM, single-particle states are Anderson localized [17] effectively, leading to many-body localization (MBL) [18,19]. The paradigm of localization in the absence of external disorder goes back to two-constituent systems (light-heavy particles) [20] and has currently resurfaced in fracton phases of matter [21] with numerous applications on lattice gauge models and more [22–32].

While transition metal compounds with a Kramers doublet due to strong spin-orbit coupling are good candidates for realizing the KSM [33–35], a proximate Kitaev-QSL is the closest that has been reported so far [36–43]. Perhaps the strongest evidence for the existence of the Kitaev-QSL has been allegedly reported in thermal Hall measurements of the $\alpha - RuCl_3$ compound [44]. However, the origin of this Hall effect and its confirmation are under active investigation [45–49]. In addition to that, longitudinal thermal transport has also been used to understand the nature of the excitations in these systems [50–53].

A valuable alternative for realizing the KSM might occur in cold atom experiments where compass interactions can be engineered [54]. Furthermore, optical lattices are also advancing the experimental study of nonergodic systems exhibiting MBL [55]. Remarkably, the demonstration for realizing lattice gauge models with $\mathbb{Z}_2$ gauge fields coupled to 1D fermions has recently been reported [56]. Thus, all three fascinating fields of Kitaev-QSL, MBL, and lattice gauge models that will be discussed in this work share the prospect of experimental materialization.

Here we present results on the 1D-KSM including a uniform external magnetic field. First, using the specific heat we show that fluxes have a clear imprint to the specific heat. At weak magnetic fields, the effective fermionic representation still holds, with the magnetic field accounting for an additional next-nearest-neighbor (NNN), time-reversal symmetry (TRS) breaking term. Violating time invariance in the context of Anderson localization could lead to delocalization due to avoiding multiple scattering events and thus reducing interference effects [57]. Our results on the inverse participation ratio (IPR) as well as transport coefficients exclude this scenario. For larger magnetic fields, we are able to detect a delocalization transition, diagnosed by finite dc transport coefficients. This is, however, attributed to different physics, namely, to the mobility of the fluxes. Some features of our results on thermal transport could possibly also relate to the longitudinal thermal transport of the 2D model.

Our paper is organized as follows. First, in Sec. II, we explain the model and its basic properties. Second, we present results on the IPR in Sec. III. Third, we detail our findings for the energy transport in the frequency domain within the effective fermionic representation in Sec. IV A and within

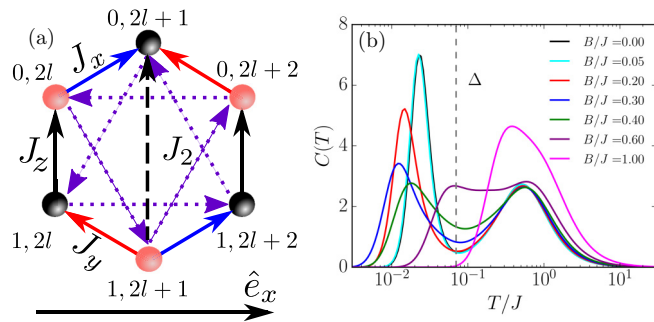*a.metavitsiadis@tu-bs.de
†w.brenig@tu-bs.de

FIG. 1. (a) A three-rung unit cell of the spin-1/2 Kitaev ladder. The direction of the arrows indicates the order of the Majorana pairs in the fermionic representation. The black dashed bond on rung $2l + 1$, connecting the zeroth and the first chains, comes from boundary conditions in the rung direction. The $\hat{e}_x$ vector emphasizes the 1D character of the model. (b) Specific heat versus temperature for different values of the magnetic field B. The data are obtained via ED in the spin representation for a system of $L = 8$ rungs (i.e., 16 spins).

the original spin representation in Sec. IV B. Finally, the energy current correlation in the time domain is presented in Sec. IV C, and we conclude in Sec. V. In Appendix A, we show more results for the IPR and the correlation function for an additional set of exchange couplings. In Appendix B, we clarify technical points regarding the energy current operator. Finally in Appendix C, we detail the extraction of the dc limit of the energy current correlation function.

II. MODEL

The KSM model describes bond-directional Ising interactions between spin $S = 1/2$ operators [4]. Its Hamiltonian in the presence of a magnetic field is given by (see also Fig. 1)

$$H_S = \sum_{\langle i,j \rangle} J_{ij}^a S_i^a S_j^a + g\mu_B \mathbf{B} \cdot \sum_j \mathbf{S}_j, \qquad (1)$$

with J_{ij}^a the Kitaev interactions ($a = x, y, z$), i, j the nearest-neighbor's (NN) sites on the lattice, $g = 1$ is the g-factor, $\mu_B = 1$ the Bohr magneton, and $\mathbf{B} = (B, B, B)$ the magnetic field. We also set to unity the Planck and Boltzmann constants $\hbar$, $k_B = 1$. The J_z-bonds in the middle of the hexagon arise from boundary conditions in the rung direction. Although the absence of these terms in Heisenberg Hamiltonians might give rise to new physics [58], here they are not expected to play any role.

For $B = 0$, KSM is characterized by a macroscopic number of local conservation laws, the so-called flux (or vison) operators and due to that it becomes analytically solvable. The ground-state sector resides in the uniform flux sector which is separated from other sectors by a gap Δ. Here we fix the Kitaev couplings to $J_x = 2J$ and $J_y = J_z = J$, where the ground state is gapless, and we numerically determine $\Delta \simeq 0.07J$. For results at different couplings, see Appendix A.

At finite temperatures, the fluxes become thermally excited and a flux proliferation process occurs for $T < \Delta$. This behavior can be read off from the specific heat, $C(T) = (\langle H_S^2 \rangle - \langle H_S \rangle^2)/T^2$, which is shown in Fig. 1(b) for different

values of the magnetic field B [59,60]. The results are obtained from exact diagonalization for an $L = 8$ rung system. For $B = 0$, it exhibits the characteristic two-peak structure of Kitaev systems [61–65]. The low-temperature peak is associated with the flux proliferation, where the system gets flooded with flux excitations. The action with the Zeeman term creates an effective hopping term for the visons, making them effectively mobile [66]. For $B < \Delta$, $C(T)$ remains practically unaffected, indicating that the picture of the fluxes still holds. Intermediate magnetic fields reduce the height of the low-T peak, which initially moves toward lower temperatures, characterizing a regime where visons are still present albeit mobile. For stronger B's, the low-temperature peak shifts to higher temperatures until it disappears, illustrating the absence of any trace of the fluxes.

Treating the magnetic field perturbatively for $B < \Delta$ enables a fermionic representation where spin operators are mapped into two species of Majorana fermions c and $\bar{c}$ [4,67], with $\{c_i, c_j\} = 2\delta_{ij} = \{\bar{c}_i, \bar{c}_j\}$ and $\{c_i, \bar{c}_j\} = 0$. One of the two species, say c, is itinerant, while the other pair up along the z-bond direction, they commute with the Hamiltonian, and they become static. We denote these local conservation laws with $\eta_j^z = \pm 1$ while we also introduce $\eta_j^x = \eta_j^y = 1$ to unify the notation. The ground state occurs for $\eta_j^z = 1$ while for $T \gg \Delta$ η_j^z is completely disordered, $\langle \eta^z \rangle = 0$. The magnetic field accounts for a TRS-breaking, NNN-interaction term in the fermionic representation, i.e., $H_S \approx H_F$ with

$$H_F = -\frac{i}{4} \sum_{\langle i,j \rangle} J_{ij}^a \eta_i^a c_i c_j - i\frac{J_2}{8} \sum_{\langle\langle i,j \rangle\rangle} \tilde{\eta}_{ij} c_i c_j, \qquad (2)$$

and $J_2 \sim \frac{B^3}{\Delta^2}$ [4,67,68]. The double angled brackets in the second term denote summation over NNN sites and the order of the majorana pairs can be read off from Fig. 1(a). For $\tilde{\eta}$ holds: $\tilde{\eta}_{ij} = 1$ for intrachain bonds or $\tilde{\eta}_{ij} = \eta_i^z + \eta_j^z$ for interchain bonds. In terms of Dirac fermions [10,37,69–71], H_F becomes a superconducting Hamiltonian on a two-site unit cell chain of length L, in the presence of an onsite $\mathbb{Z}_2$ gauge field $\sim\eta_j^z$, as well as bond disorder terms $\sim\tilde{\eta}_{ij}$.

III. INVERSE PARTICIPATION RATIO

The first quantity that we look at in order to detect localization is the IPR, which is given by the sum over the lattice sites of the squared probabilities of the wave functions ψ [72]. For a given η-configuration, we denote the average IPR with I_η, while for disordered sectors, we average over R gauge configurations to obtain the moments $\mathcal{I}_p$, viz.,

$$I_\eta = \frac{1}{L} \sum_{m=1}^{L} \sum_{l=1}^{L} \left| \psi_m^\eta(l) \right|^4, \quad \mathcal{I}_p = \frac{1}{R} \sum_{r=1}^{R} (I_{\eta_r})^p. \qquad (3)$$

From these definitions, the mean IPR is given by $\bar{I} = \mathcal{I}_1$, while the fluctuations around this mean can be quantified via the standard deviation $\sigma = \sqrt{\delta\bar{I}/R}$, where $\delta\bar{I} = \mathcal{I}_2 - (\mathcal{I}_1)^2$.

Assuming that all states of a system are localized $\psi_m^\eta(l) \sim \delta_{lm}$, the IPR is expected to scale as $\bar{I}(L) \sim$ const, while for extended states $\psi_m^\eta(l) \sim 1/\sqrt{L}$, $\bar{I}(L) \sim 1/L$. In Fig. 2(a), we plot in a log-log scale the IPR of the uniform gauge sector for different values of the J_2 coupling versus the system size,
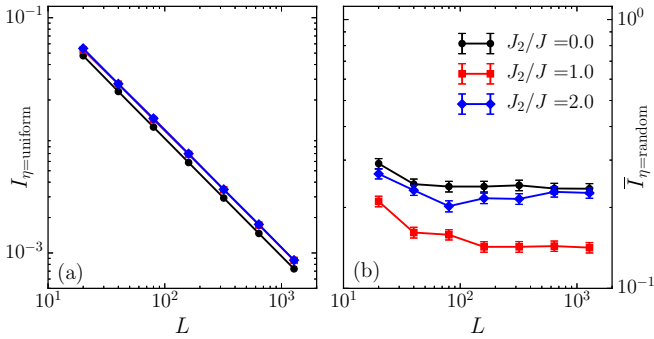
FIG. 2. System-size scaling of the IPR of the fermionic model, Eqs. (2) and (3), in a log-log scale for different values of the J_2 coupling. (a) Uniform gauge configuration. (b) Random average over $R = 1000$ maximally disordered states, $\langle \eta^z \rangle = 0$, and 3σ are depicted as error bars.

which reveals a $\sim 1/L$ scaling. On the contrary, for the same values of J_2, random averaging η^z over $R = 1000$ configurations, with $\langle \eta^z \rangle = 0$ [73], reveal the opposite behavior, namely $\bar{I}(L) \sim$ const. The difference between "clean" and "dirty" sectors is striking and elucidates the localization character of the disordered states for any J_2. The initial drop of the IPR in Fig. 2(b) can be attributed to a comparable localization length ξ with the system size. Moreover, from this behavior, it is hard to conclude a large sensitivity of ξ to J_2.

IV. ENERGY TRANSPORT

Next we study the dynamical transport properties of H_F. For that, we employ the energy current dynamical autocorrelation function, which has the advantage to be diagonal in the gauge fields, and it is also directly related to the experimentally measurable thermal conductivity,

$$\mathcal{C}(t) = \frac{1}{L} \langle j^{\epsilon}(t) j^{\epsilon} \rangle, \quad \mathcal{C}(\omega) = \int dt \, e^{i\omega t} \mathcal{C}(t). \quad (4)$$

Here, j^{ϵ} is the energy current operator, the exact expression of which is acquired via the time derivative of the polarization operator $j^{\epsilon} = \frac{\partial P}{\partial t}$, $P = \sum_l r_l h_l$, with h_l being a local energy density [74–76] and r_l its corresponding coordinate. See Appendix B for more details. The angled brackets denote a thermal expectation value, which here is restricted to infinite temperature to improve statistics, however, our qualitative conclusions should hold for intermediate to high temperatures, i.e., $T > \Delta$. For the discussion of localization we are interested in the low-ω properties of $\mathcal{C}(\omega)$, and mainly its static part, which comprises two contributions: (i) The Drude weight arising from the nonvanishing due to degeneracies part of the correlation function at longer times, $2\pi \mathcal{C}_0 = \lim_{t \to \infty} \mathcal{C}(t)$; (ii) the dc limit of the regular part $\mathcal{C}_{dc} = \lim_{\omega \to 0} \mathcal{C}(\omega)$. The former indicates ballistic while the latter indicates dissipative transport and if both of them vanish, the system is an insulator.

A. Fermionic representation

In Fig. 3(a), we present results for $\mathcal{C}(\omega)$, acquired via ED in the fermionic representation [13], for different values of
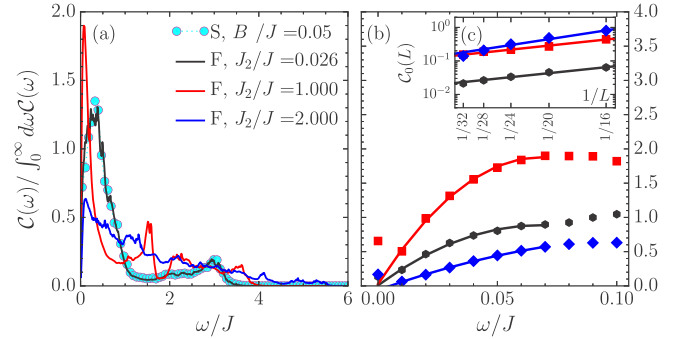

FIG. 3. (a) Frequency dependence of the energy current correlation function in the fermionic representation, Eq. (2), for $J_2/J = 0.026, 1, 2$ and $L = 32$. Data are binned in windows of $\delta\omega = 0.01J$. For comparison, $\mathcal{C}(\omega)$ evaluated with H_S, for $B = 0.05J$, and $L = 8$ is also shown marked with cyan circles connected by a dotted line. (b) A zoom at low frequencies of (a). The lines depict second-order polynomials fitted in the range $0 < \omega/J < 0.07$ to extract the dc limit. (c) Finite-size scaling of the Drude weight $\mathcal{C}_0$, in a semilog plot. The lines are exponential fits.

the NNN interaction and $L = 32$, corresponding to a Hilbert space dimension of 2^{64}. Due to the different energy scales, we normalize the curves to a unit integral. In the fermionic representation, the quadratic form of H_F yields two types of contributions in $\mathcal{C}$, "quasiparticle" or "pair-breaking." These can be discerned in the curve for $J_2 = 0.026J$, corresponding to $B = 0.05J < \Delta$. First, the maximum around $\omega \approx 0.4J$ is attributed to the quasiparticle part of the correlation function. The sharp decrease of $\mathcal{C}(\omega)$ at lower frequencies, $\omega \lesssim 0.2J$, better highlighted in Fig. 3(b), is inevitable due to the localization of the single-particle states. Exactly the same behavior is recovered in the spin representation from the many-body Hamiltonian H_S, also plotted in Fig. 3(a), for $B/J = 0.05$, and $L = 8$. Second, the broader and of lower intensity hump, centered around $\omega \approx 3J$, corresponds to the pair-breaking type of contributions. As J_2 is further increased, the gap between the quasiparticle and the pair-breaking contributions is filled, however, as better seen in Fig. 3(b), the pseudogap at low frequencies does not close.

In Fig. 3(b), we highlight the low frequency behavior of $\mathcal{C}(\omega)$ for the fermionic spectra plotted in panel (a). The lines connecting the points are second-order polynomial fits in the range $0 < \omega/J < 0.07$ and extrapolate to tiny or even negative values at $\omega = 0$ [77]. A small Drude weight $\mathcal{C}_0$ also becomes visible in Fig. 3(b), which finite-size scaling behavior is plotted in Fig. 3(c) for systems $L = 16 - 32$. The lines are exponential fits to the data and imply an exponential decay of $\mathcal{C}_0$, namely, $\mathcal{C}_0 \to 0$ for $L \to \infty$. Thus, it can be inferred that both $\mathcal{C}_0$ and $\mathcal{C}_{dc}$ vanish in the thermodynamic limit.

To summarize our findings thus far, and as one of our prime conclusions, results for both quantities the IPR and the $\mathcal{C}(\omega)$ indicate that a delocalization of the system cannot be captured within the fermionic representation despite the TRS-breaking nature of the NNN interaction induced by the magnetic field.

B. Spin representation

Next, we contrast the previous findings to $\mathcal{C}(\omega)$ obtained within the H_S framework, where the magnetic field is taken
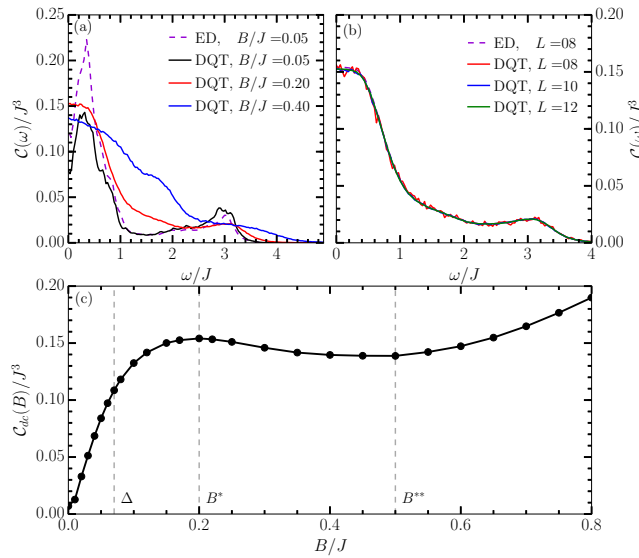
FIG. 4. (a) Frequency dependence of the energy current correlation function in the spin representation, Eq. (1) for different values of the magnetic field, with $L = 8$ and $\delta\omega = 0.05J$ for the ED data, while $L = 12$ and $\delta\omega = \pi J/100$ for the DQT ones. (b) Finite-size scaling of $\mathcal{C}(\omega)$ for $B = 0.2J$. (c) $\mathcal{C}_{dc}(B)$ versus the magnetic field. The gray dashed lines indicate the three characteristic energy scales $B \approx \Delta, B^*, B^{**}$.

fully into account [Eq. (1)]. To improve on the available system sizes, facing the complete many-body Hilbert space, and in addition to ED, we also employ Dynamical Quantum Typicality (DQT). In DQT a thermal mean value is approximated by an expectation value obtained from a single pure random state $|\psi\rangle$, drawn from a distribution that is invariant under all unitary transformations in Hilbert space (Haar measure), which leads to an exponential error decrease with L [78]. The real part of correlation function is then evaluated via $\mathcal{C}'(t) \approx$ Re $\frac{\langle\psi|j(t)j|\psi\rangle}{L\langle\psi|\psi\rangle}$ by solving a standard differential equation problem for the time evolution. The time evolution is performed with a $J\delta t = 0.01$ step [corresponding to an accuracy of the order of $O(10^{-8})$ in the fourth order Runge-Kutta algorithm], while we integrate for times up to $Jt_{\max} = 100$, yielding a frequency resolution of $\delta\omega = \pi J/t_{\max}$.

Since DQT yields only the real part of the correlation function in the time domain, to obtain the frequency spectra we consider the quantity,

$$\tilde{\mathcal{C}}(\omega) = \int_0^\infty dt \cos(\omega t)\mathcal{C}'(t). \quad (5)$$

After some algebra, one can show that $\mathcal{C}(\omega)$ and $\tilde{\mathcal{C}}(\omega)$ are related via

$$\tilde{\mathcal{C}}(\omega) = \frac{1}{2}(1 + e^{-\beta\omega})\mathcal{C}(\omega); \quad (6)$$

therefore, at high temperatures $\beta J \ll 1$, the two quantities are identical.

The results for $\mathcal{C}(\omega)$ for different values of B are presented in Fig. 4(a). For additional data at the isotropic point, $J_{x,y,z} = J$, see Appendix A. First, comparing DQT ($L = 12$) and ED ($L = 8$) at weak magnetic fields reveals a discrepancy between the two methods. This is due to the long time os-
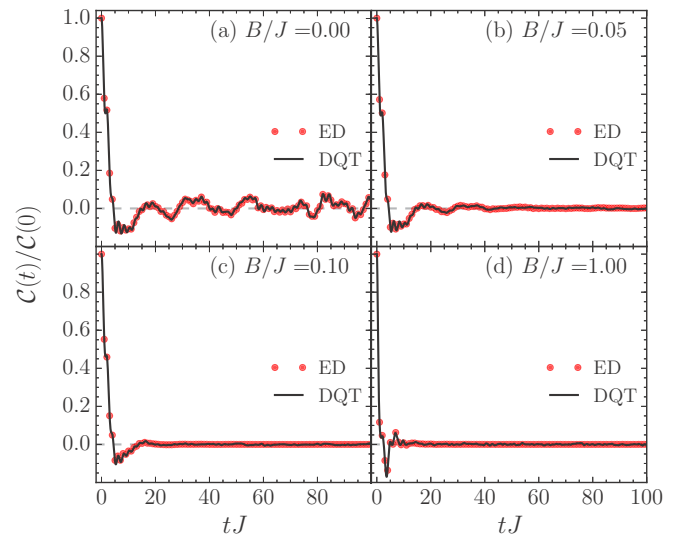

FIG. 5. Comparison of the dynamical energy current correlation function $\mathcal{C}(t)$ obtained via ED or DQT for different values of the magnetic field $B/J = 0, 0.05, 0.1, 1$. Data are obtained on ladders with $L = 8$ rungs at $\beta = 0$.

cillations of the Kitaev terms, causing $\mathcal{C}(t)$ to oscillate even at the longest times kept here. These discrepancies disappear at higher magnetic fields where $\mathcal{C}(t_{\max}) = 0$ and do not invalidate any of our conclusions; see also Figs. 4(b) and 5 and the discussion in Sec. IV C. At low magnetic field, we observe a very rapid filling of the low-frequency depletion. This can be interpreted as a large weakening of the fluxes' scattering strength once they become mobile. Already at $B = 0.2J$, the low-frequency depletion disappears giving $\mathcal{C}(\omega)$ a more Drude-like shape, although the higher frequency pair-breaking structure can still be observed. For even higher values of the magnetic field, higher and lower frequencies are smoothly connected. In Fig. 4(b), we present the finite-size scaling behavior of $\mathcal{C}(\omega)$, also comparing ED and DQT. We find that there are practically no finite-size effects at moderate magnetic fields in the data of the spin representation.

Last, in Fig. 4(c), we highlight the behavior of the dc limit $\mathcal{C}_{dc}(B) = \mathcal{C}(\omega \to 0, B)$ versus the magnetic field. The dc limit is acquired by second-order polynomial fit at the low-frequency data for a frequency resolution of $\delta\omega = 0.05J$ and displays three distinct regimes. First, $\mathcal{C}_{dc}$ exhibits a very steep increase for weak magnetic fields, $B \lesssim \Delta$, while it continues to gradually grow until it reaches a local maximum around $B^* \approx 0.2J$. We interpret this as a characteristic energy scale required for the fluxes to become sufficiently mobile. The finite value of $\mathcal{C}_{dc}$ for $B \lesssim \Delta$ on a finite system is to be expected and does not contradict our previous findings. Second, for intermediate magnetic fields, $B^* \lesssim B \lesssim B^{**}$ with $B^{**} \approx 0.5J$, $\mathcal{C}_{dc}$ varies very slowly with magnetic field, indicating a delocalized two component system. Third, for strong magnetic fields, $B \gtrsim B^{**}$, $\mathcal{C}_{dc}$ grows again, signaling a regime with primarily magnetothermal contributions [16].

C. Time domain

Here we want to further elaborate on the difference between ED and DQT, at weak magnetic fields, as this is

manifested in the $\mathcal{C}(\omega)$ spectrum [Fig. 4(a)]. To understand the origin of this, we consider the energy current correlation function in the time domain $\mathcal{C}(t)$. In Fig. 5, we present results for $\mathcal{C}(t)$ obtained either via ED or via DQT for different values of the magnetic field. From these data, it becomes apparent that there is an excellent agreement between the two methods in the time domain, for any value of the magnetic field. Moreover, these additional results clarify the origin of the difference in Fig. 4(a) directly. In fact, at low fields $\mathcal{C}(t)$ displays oscillations which do not decay within the accessible time window. This renders the Fourier transform $t \rightarrow \omega$ of the DQT data inaccurate. For ED, the ω-data in Fig. 4 are evaluated directly in the frequency domain and therefore do not suffer from this artifact. For weak magnetic fields, the spectrum resembles more like that of the pure Kitaev model, which exhibits a large degree of degeneracy. This is the origin of the nondecaying, and oscillatory part of the correlation function [Figs. 5(a) and 5(b)]. For stronger magnetic fields, however [Figs. 5(c) and 5(d)], the correlation time is short, causing no problem in Fourier transforming the time domain data.

V. DISCUSSION

Our main finding here is that fractionalization in the 1D-KSM, leading to a thermally activated flux disorder, induces self-localization for $B \lesssim \Delta$ and therefore leads to vanishing thermal transport coefficients. For stronger magnetic fields $B \gtrsim \Delta$, flux mobility and many-body interactions fill the low-frequency depletion of $\mathcal{C}(\omega \ll 1)$ leading to delocalization and finite transport coefficients. The absence of this behavior in the popular simplification of the 1D-KSM, which treats magnetic fields only perturbatively, raises questions on the applicability of the latter model to describe finite-field transport.

Let us now *speculate* on the implications of our results for the 2D-KSM, since the two models share very similar properties [10]. The characteristic low-frequency depletion, attributed to the scattering of fermions on the gauge field [12,13], is also a characteristic of the 2D-KSM [64,79,80]. An essential difference in the absence of magnetic field between the 1D- and the 2D-KSM is that in the latter, the pseudo-gap closes in the thermodynamic limit restoring dc transport. However, it is plausible to assume that the mechanism of filling the low-frequency depletion in the $\mathcal{C}(\omega)$ spectra due to the flux mobility should also be present in 2D. One could even go so far as to claim that the energy scales at which this would happen would be similar with the ones presented here, since the flux gap for the 1D and the 2D systems is almost equal, $\Delta_{2D} \approx \Delta = 0.07J$. Whether or not these speculations actually become manifest in the 2D-KSM and more so in the longitudinal thermal transport of Kitaev materials is an open question for future research.

APPENDIX A: GAPPED PHASE

Whereas for the main part of the manuscript we have set the Kitaev couplings such as to remain in the gapless phase, in this section, we discuss the IPR and the correlation function for a different set of exchange couplings. Here we consider the isotropic limit, namely $J_{x,y,z} = J$.

First, in Fig. 6, the IPR is plotted for a uniform η-configuration, panel (a), while random averaged IPR's are presented in panel (b). The uniform-gauge sectors exhibit an $\sim 1/L$ decay of the IPR while the disordered sectors saturate to some constant value. These findings are in accordance with the results of the main text for $J_x = 2J, J_y = J_z = J$ and support the self-localization picture described in the main text, also for different sets of exchange couplings.

Second, results for the correlation function, derived in the spin representation, at different magnetic fields, and at $\beta = 0$, are plotted in Fig. 7. For comparison, we also plot the corresponding results for the coupling set $J_{x,y,z} = 2J, J, J$ and we normalize the frequency axis by $\mathcal{J}$ and the correlation function by $\mathcal{J}^3$, where $\mathcal{J} = (J_x + J_y + J_z)/3$ is the "average" energy scale. For all values of the magnetic field, the correlation function behaves similarly for the two coupling sets. Some quantitative differences can be observed at large magnetic fields.

APPENDIX B: ENERGY CURRENT OPERATOR

Here we list the technical steps necessary to obtain the energy current operator. In doing so, we also clarify two additional conceptional details. First, as any current, also the energy current is related to a local density, i.e., the local energy density h_l in our case. As for any such density, for which the only requirement is that its sum over the "sites" l, i.e., $\sum_l h_l = H$, yields an extensive quantity, the energy density is not defined uniquely. Typically, strongly local combinations of operators are chosen for h_l. The current correlation functions
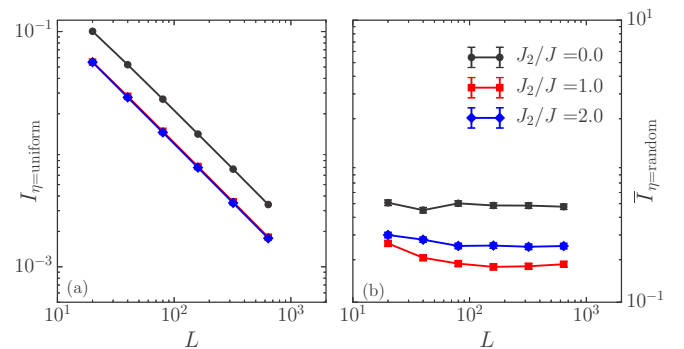

FIG. 6. System size scaling of the IPR of the fermionic model, for $J_x = J_y = J_z = J$. Results are presented in a log-log scale for different values of the J_2 coupling. Uniform gauge configurations are depicted in panel (a) while disordered ones in (b). We perform a random average over $R = 1000$ maximally disordered states and include 3σ as error bars.
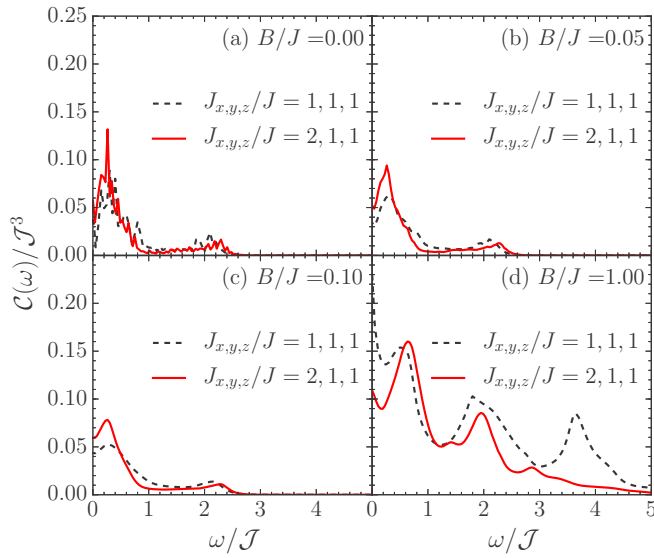
FIG. 7. Frequency dependence of the current correlation function for different values of the magnetic field, $B/J = 0, 0.05, 0.1, 1$, and comparing two coupling sets, $J_{x,y,z}/J = 1, 1, 1$ and $J_{x,y,z}/J = 2, 1, 1$. Results are obtained via ED on $L = 8$ rungs at $\beta = 0$ and for $\delta\omega = 0.05J$. The x, y-axes are normalized with $\mathcal{J}$ and $\mathcal{J}^3$, respectively, where $\mathcal{J} = (J_x + J_y + J_z)/3$.

for two distinct choices of energy densities will typically *not* agree at high frequencies, where the short-range structure of the energy density chosen starts to play a role. However, at low frequencies, one typically finds agreement. We will explicitly detail such behavior for two choices of the energy density operator. For the second conceptual detail, we show that the current can either be evaluated via the time dependence of the energy polarization operator or via the continuity equation. We will clarify their relation and show examples of both.

1. Polarization operator

First, we use the energy polarization operator P^ϵ, where the energy current operator j^ϵ is determined from the time derivative of P^ϵ [81],

$$j^\epsilon = i[H, P^\epsilon], \quad P^\epsilon = \sum_l r_l h_l, \quad H = \sum_l h_l. \quad \text{(B1)}$$

FIG. 8. The two different energy densities considered here for the Kitaev ladder. Blue, red, and black bonds indicate J_x, J_y, and J_z Kitaev interactions respectively.

Here r_l is the coordinate of the given local energy density h_l and l runs over all such lattice segments. In other words, the energy current operator depends on how the system's local energy density h_l is defined. The Kitaev ladder has a complicated two-rung unit cell which allows for two natural choices of h_{2l}, regarding the J_z-bonds; see also Fig. 8. First, we consider a symmetrization scheme for the XY-bonds, while we parametrize the two choices on the J_z-bonds in terms of the c_1, c_2 coefficients, i.e.,

$$
\begin{aligned}
h_{2l} = \frac{J_z}{2} \big(& S^z_{1,2l} S^z_{2,2l} + c_1 S^z_{1,2l+1} S^z_{2,2l+1} \\
& + S^z_{1,2l+2} S^z_{2,2l+2} + c_2 S^z_{1,2l+3} S^z_{2,2l+3} \big) \\
& + \frac{J_x}{2} \big(S^x_{1,2l} S^x_{1,2l+1} + S^x_{1,2l+2} S^x_{1,2l+3} + 2 S^x_{2,2l+1} S^x_{2,2l+2} \big) \\
& + \frac{J_y}{2} \big(S^y_{2,2l} S^y_{2,2l+1} + S^y_{2,2l+2} S^y_{2,2l+3} + 2 S^x_{1,2l+1} S^x_{1,2l+2} \big),
\end{aligned}
\quad \text{(B2)}
$$

where $c_1 = 2$, $c_2 = 0$ for h^A_{2l}, and $c_1 = c_2 = 1$ for h^B_{2l} of Fig. 8. The energy density h^A_{2l} is the one used in the paper. For each case, we need to also take into account the Zeeman energy density yielded by the magnetic field. For that, we add to the energy density of Eq. (B2) the term

$$h_{Z,2l} = \frac{1}{2} \sum_{\nu=1}^{2} \sum_{j=0}^{3} \mathbf{B} \cdot \mathbf{S}_{\nu,2l+j}, \quad \text{(B3)}$$

where ν sums over the two chains and j the sites of the energy densities. The total energy density is the sum $h_{2l} + h_{Z,2l}$.

From Eq. (B1), the energy current operators for both energy densities are simply evaluated to arrive at

$$
\begin{aligned}
j^\epsilon_A = \sum_{l=0}^{L/2-1} \Big[& 2J_x J_y \big(S^x_{1,2l+1} S^y_{1,2l-1} S^z_{1,2l} - S^x_{2,2l-1} S^y_{2,2l+1} S^z_{2,2l} \big) + 2J_z \big(J_x S^x_{1,2l} S^y_{1,2l+1} S^z_{2,2l+1} - J_y S^x_{2,2l+1} S^y_{2,2l} S^z_{1,2l+1} \big) \\
& + J_x \big[B_z \big(S^x_{2,2l+1} S^y_{2,2l+2} - S^x_{2,2l+2} S^y_{2,2l+1} \big) - B_y \big(S^x_{2,2l+1} S^z_{2,2l+2} - S^x_{2,2l+2} S^z_{2,2l+1} \big) \big] \\
& - J_y \big[B_z \big(S^y_{1,2l+1} S^x_{1,2l+2} - S^y_{1,2l+2} S^x_{1,2l+1} \big) - B_x \big(S^y_{1,2l+1} S^z_{1,2l+2} - S^y_{1,2l+2} S^z_{1,2l+1} \big) \big] \\
& + J_z \big[B_x \big(S^z_{1,2l} S^x_{2,2l} + S^z_{2,2l} S^x_{1,2l} \big) - B_y \big(S^z_{1,2l} S^y_{2,2l} + S^z_{2,2l} S^y_{1,2l} \big) \big] \Big]
\end{aligned}
\quad \text{(B4a)}
$$

$$
\begin{aligned}
j^\epsilon_B = \sum_{l=0}^{L/2-1} \Big[& 2J_x J_y \big(S^x_{1,2l+1} S^y_{1,2l-1} S^z_{1,2l} - S^x_{2,2l-1} S^y_{2,2l+1} S^z_{2,2l} \big) \\
& + J_z \big[J_x \big(S^x_{2,2l-1} S^y_{2,2l} S^z_{1,2l} - S^x_{2,2l+2} S^y_{2,2l+1} S^z_{1,2l+1} \big) + J_y \big(S^x_{1,2l+1} S^y_{1,2l+2} S^z_{2,2l+1} - S^x_{1,2l} S^y_{1,2l-1} S^z_{2,2l} \big) \big] \\
& + J_x \big[B_z \big(S^x_{2,2l+1} S^y_{2,2l+2} - S^x_{2,2l+2} S^y_{2,2l+1} \big) - B_y \big(S^x_{2,2l+1} S^z_{2,2l+2} - S^x_{2,2l+2} S^z_{2,2l+1} \big) \big] \\
& - J_y \big[B_z \big(S^y_{1,2l+1} S^x_{1,2l+2} - S^y_{1,2l+2} S^x_{1,2l+1} \big) - B_x \big(S^y_{1,2l+1} S^z_{1,2l+2} - S^y_{1,2l+2} S^z_{1,2l+1} \big) \big] \Big].
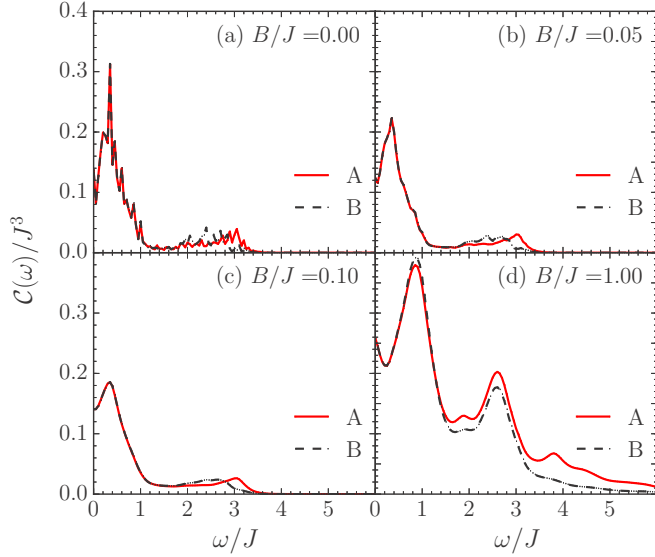\end{aligned}
\quad \text{(B4b)}
$$

FIG. 9. Comparison of the dynamical energy current correlation function $\mathcal{C}(\omega)$ for the two energy densities considered in Fig. 8, leading to Eqs. (B4). We present data for four different values of the magnetic field $B/J = 0, 0.05, 0.1, 1$ at $\beta = 0$ via ED for a system of $L = 8$ rungs and $\delta\omega = 0.05J$.

Here we have used the translation symmetry of the ladder by two sites, $\mathbf{S}_{\nu,j} \to \mathbf{S}_{\nu,j\pm2}$, as well as the translation by one site combined with a leg inversion, $\mathbf{S}_{\nu,j} \to \mathbf{S}_{\bar{\nu},j\pm1}$, where $\nu = 1(2)$ and $\bar{\nu} = 2(1)$, respectively. This allows for a nonunique way of rewriting the above terms, while respecting the lattice symmetries. The last two terms are a result of the way that the J_z bonds are taken into account and vanish for the second convention of the energy density.

2. Continuity equation

An alternative way to determine the current operator is via the long wavelength limit of the continuity equation

$$\frac{\partial h_q}{\partial t} \sim -iq j^\epsilon, \quad \text{for} \quad q \to 0. \tag{B5}$$

First, we emphasize that inserting the Fourier transform $h_q = \sum_l e^{iqr_l} h_l$ using the definitions of r_l and h_l from Eq. (B1) into the continuity equation, one obviously regains j^ϵ from Eq. (B1) for $q \to 0$, i.e. these approaches are *equivalent*. Second, in the literature [75], it is popular to use a version of h_q obtained by summing all bonds or on-site energies with the "appropriate" Fourier factor, i.e.,

$$h_q = \sum_{l=0}^{L/2-1} \left[e^{iq(2l+\frac{1}{2})} \left(J_x S_{1,2l}^x S_{1,2l+1}^x + J_y S_{2,2l}^y S_{2,2l+1}^y \right) \right.$$
$$\left. + e^{iq(2l+\frac{3}{2})} \left(J_x S_{2,2l+1}^x S_{2,2l+2}^x + J_y S_{1,2l+1}^y S_{1,2l+2}^y \right) \right]$$
$$+ \sum_{l=0}^{L-1} e^{iql} \left[J_z S_{1,l}^z S_{2,l}^z + \mathbf{B} \cdot (\mathbf{S}_{1,l} + \mathbf{S}_{2,l}) \right]. \tag{B6}$$

It is reassuring to realize, that this h_q simply encodes yet another a priori choice of local energy densities and corre-
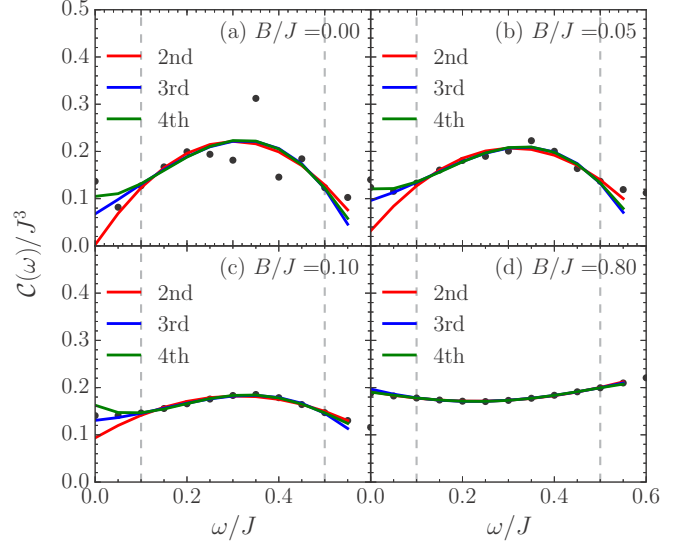

FIG. 10. Low-frequency spectra of $\mathcal{C}(\omega)$ (points), obtained via ED on $L = 8$ rungs at $\beta = 0$, for different values of the magnetic field $B/J = 0, 0.05, 0.1, 0.8$. The full frequency range can be seen in Fig. 9. The solid lines depict polynomial fits of 2nd, 3rd, and 4th degree, while the gray dashed lines indicate the region of the fitting procedure.

sponding polarization operators, namely $H = \sum_{l\mu} h_{l\mu}$, with $h_{l1,2,3,4} = (J_x S_{1,2l}^x S_{1,2l+1}^x + J_y S_{2,2l}^y S_{2,2l+1}^y)$, $(J_x S_{2,2l+1}^x S_{2,2l+2}^x + J_y S_{1,2l+1}^y S_{1,2l+2}^y)$, $J_z S_{1,2l}^z S_{2,2l}^z + \mathbf{B} \cdot (\mathbf{S}_{1,2l} + \mathbf{S}_{2,2l})$, and $J_z S_{1,2l+1}^z S_{2,2l+1}^z + \mathbf{B} \cdot (\mathbf{S}_{1,2l+1} + \mathbf{S}_{2,2l+1})$, as well as $P^\epsilon = \sum_{l\mu} r_{l\mu} h_{l\mu}$, with $r_{l1,2,3,4} = 2l + 1/2, \quad 2l + 3/2, 2l$, and $2l + 1$. Interestingly, using Eq. (B6) we arrive at the same energy current as in Eq. (B4b), which highlights that different P^ϵ can lead to identical j^ϵ.

In Fig. 9, we present results for $\mathcal{C}(\omega)$ for the two different energy densities, shown in Fig. 8, leading to the energy current operators of Eqs. (B4a) and (B4b). In each panel of Fig. 9, a different value of the magnetic field is chosen, while we keep $\beta = 0$. The data are obtained via ED on a system of $L = 8$ rungs and we bin the δ-functions in bins of width $\delta\omega = 0.05J$. The data of Fig. 9 support our argument of the main text, namely, that different conventions for the energy current operator lead to small deviations at higher frequencies but they barely affect the low-frequency $\mathcal{C}(\omega)$ spectra. Note that the deviations at higher frequencies are more prominent at higher magnetic fields.

APPENDIX C: THE DC LIMIT

In this section, we discuss the extrapolation to the dc limit of the frequency dependent correlation function $\mathcal{C}_{dc} = \mathcal{C}(\omega\to0)$. For intermediate magnetic fields $B \gtrsim 0.1J$, and up to very strong magnetic fields $B \approx J$, the correlation function acquires a rather smooth low-frequency shape, which allows for a safe extrapolation of the $\omega \to 0$ limit. For weaker magnetic fields $B \lesssim \Delta$ however, the correlation function develops a sharp dip at low frequencies rendering the dc-limit extrapolation rather challenging. We stress that while here we merely exemplify the procedure for the spin representation, in the

weak-B regime, one can also rely on the fermionic representation of the model to perform finite-size analysis for very large systems.

In Fig. 10, we present the dc-limit extrapolation for a wide range of magnetic field values and using polynomials of different degrees. First, we see that only at weak magnetic fields, different polynomials give small quantitative differences. For weak magnetic fields, $B \lesssim \Delta$, $C_{dc} \neq 0$, which is a finite-size effect, as discussed in the main paper, and is in line with its main message.

---

[1] L. Savary and L. Balents, Quantum spin liquids: A review, Rep. Prog. Phys. **80**, 016502 (2017).

[2] Y. Zhou, K. Kanoda, and T.-K. Ng, Quantum spin liquid states, Rev. Mod. Phys. **89**, 025003 (2017).

[3] J. Knolle and R. Moessner, A field guide to spin liquids, Annu. Rev. Condens. Matter Phys. **10**, 451 (2019).

[4] A. Kitaev, Anyons in an exactly solved model and beyond, Ann. Phys. **321**, 2 (2006).

[5] M. Hermanns, I. Kimchi, and J. Knolle, Physics of the Kitaev model: Fractionalization, dynamic correlations, and material connections, Annu. Rev. Condens. Matter Phys. **9**, 17 (2018).

[6] P. P. Stavropoulos, D. Pereira, and H.-Y. Kee, Microscopic Mechanism for a Higher-Spin Kitaev Model, Phys. Rev. Lett. **123**, 037203 (2019).

[7] G. Baskaran, D. Sen, and R. Shankar, Spin-s Kitaev model: Classical ground states, order from disorder, and exact correlation functions, Phys. Rev. B **78**, 115116 (2008).

[8] I. Rousochatzakis, Y. Sizyuk, and N. B. Perkins, Quantum spin liquid in the semiclassical regime, Nat. Commun. **9**, 1575 (2018).

[9] Y. Motome and J. Nasu, Hunting majorana fermions in Kitaev magnets, J. Phys. Soc. Jpn. **89**, 012002 (2020).

[10] X.-Y. Feng, G.-M. Zhang, and T. Xiang, Topological Characterization of Quantum Phase Transitions in a Spin-1/2 Model, Phys. Rev. Lett. **98**, 087204 (2007).

[11] N. Wu, Topological phases of the two-leg Kitaev ladder, Phys. Lett. A **376**, 3530 (2012).

[12] R. Steinigeweg and W. Brenig, Energy dynamics in the Heisenberg-Kitaev spin chain, Phys. Rev. B **93**, 214425 (2016).

[13] A. Metavitsiadis and W. Brenig, Thermal transport in a one-dimensional $\mathbb{Z}_2$ spin liquid, Phys. Rev. B **96**, 041115(R) (2017).

[14] A. Metavitsiadis, C. Psaroudaki, and W. Brenig, Spin liquid fingerprints in the thermal transport of a Kitaev-Heisenberg ladder, Phys. Rev. B **99**, 205129(R) (2019).

[15] C. E. Agrapidis, J. van den Brink, and S. Nishimoto, Ground state and low-energy excitations of the Kitaev-Heisenberg two-leg ladder, Phys. Rev. B **99**, 224418 (2019).

[16] E. S. Sørensen, A. Catuneanu, J. S. Gordon, and H.-Y. Kee, Heart of Entanglement: Chiral, Nematic, and Incommensurate Phases in the Kitaev-Gamma Ladder in a Field, Phys. Rev. X **11**, 011013 (2021).

[17] P. W. Anderson, Absence of diffusion in certain random lattices, Phys. Rev. **109**, 1492 (1958).

[18] R. Nandkishore and D. A. Huse, Many-body localization and thermalization in quantum statistical mechanics, Annu. Rev. Condens. Matter Phys. **6**, 15 (2015).

[19] F. Alet and N. Laflorencie, Many-body localization: An introduction and selected topics, C. R. Phys. **19**, 498 (2018).

[20] Y. Kagan and L. A. Maksimov, Localization in a system of interacting particles diffusing in a regular crystal, Zh. Eksp. Teor. Fiz. **87**, 348 (1984) [Sov. Phys. JETP **60**, 201 (1984)].

[21] R. M. Nandkishore and M. Hermele, Fractons, Annu. Rev. Condens. Matter Phys. **10**, 295 (2019).

[22] W. De Roeck and F. Huveneers, Scenario for delocalization in translation-invariant systems, Phys. Rev. B **90**, 165137 (2014).

[23] M. Schiulaz, A. Silva, and M. Müller, Dynamics in many-body localized quantum systems without disorder, Phys. Rev. B **91**, 184202 (2015).

[24] N. Y. Yao, C. R. Laumann, J. I. Cirac, M. D. Lukin, and J. E. Moore, Quasi-Many-Body Localization in Translation-Invariant Systems, Phys. Rev. Lett. **117**, 240601 (2016).

[25] A. Smith, J. Knolle, D. L. Kovrizhin, and R. Moessner, Disorder-Free Localization, Phys. Rev. Lett. **118**, 266601 (2017).

[26] R. Mondaini and Z. Cai, Many-body self-localization in a translation-invariant hamiltonian, Phys. Rev. B **96**, 035153 (2017).

[27] H. Yarloo, A. Langari, and A. Vaezi, Anyonic self-induced disorder in a stabilizer code: Quasi many-body localization in a translational invariant model, Phys. Rev. B **97**, 054304 (2018).

[28] A. A. Michailidis, M. Žnidarič, M. Medvedyeva, D. A. Abanin, T. Prosen, and Z. Papić, Slow dynamics in translation-invariant quantum lattice models, Phys. Rev. B **97**, 104307 (2018).

[29] M. Mamaev, I. Kimchi, M. A. Perlin, R. M. Nandkishore, and A. M. Rey, Quantum Entropic Self-Localization With Ultracold Fermions, Phys. Rev. Lett. **123**, 130402 (2019).

[30] M. Brenes, M. Dalmonte, M. Heyl, and A. Scardicchio, Many-Body Localization Dynamics from Gauge Invariance, Phys. Rev. Lett. **120**, 030601 (2018).

[31] H. Yarloo, M. Mohseni-Rajaee, and A. Langari, Emergent statistical bubble localization in a $\mathbb{Z}_2$ lattice gauge theory, Phys. Rev. B **99**, 054403 (2019).

[32] P. Sala, T. Rakovszky, R. Verresen, M. Knap, and F. Pollmann, Ergodicity Breaking Arising from Hilbert Space Fragmentation in Dipole-Conserving Hamiltonians, Phys. Rev. X **10**, 011047 (2020).

[33] G. Jackeli and G. Khaliullin, Mott Insulators in the Strong Spin-Orbit Coupling Limit: From Heisenberg to a Quantum Compass and Kitaev Models, Phys. Rev. Lett. **102**, 017205 (2009).

[34] J. Chaloupka, G. Jackeli, and G. Khaliullin, Kitaev-Heisenberg Model on a Honeycomb Lattice: Possible Exotic Phases in Iridium Oxides A_2iro$_3$, Phys. Rev. Lett. **105**, 027204 (2010).

[35] H. Takagi, T. Takayama, G. Jackeli, G. Khaliullin, and S. E. Nagler, Kitaev quantum spin liquid—concept and materialization, Nat. Rev. Phys. **1**, 264 (2019).

[36] K. W. Plumb, J. P. Clancy, L. J. Sandilands, V. V. Shankar, Y. F. Hu, K. S. Burch, H.-Y. Kee, and Y.-J. Kim, α-RuCl$_3$: A spin-orbit assisted Mott insulator on a honeycomb lattice, Phys. Rev. B **90**, 041112(R) (2014).

[37] Z. Nussinov and J. van den Brink, Compass models: Theory and physical motivations, Rev. Mod. Phys. **87**, 1 (2015).

[38] A. Banerjee, C. A. Bridges, J.-Q. Yan, A. A. Aczel, L. Li, M. B. Stone, G. E. Granroth, M. D. Lumsden, Y. Yiu, J. Knolle, S. Bhattacharjee, D. L. Kovrizhin, R. Moessner, D. A. Tennant, D. G. Mandrus, and S. E. Nagler, Proximate Kitaev quantum spin liquid behaviour in a honeycomb magnet, Nat. Mater. **15**, 733 (2016).

[39] S. K. Choi, R. Coldea, A. N. Kolmogorov, T. Lancaster, I. I. Mazin, S. J. Blundell, P. G. Radaelli, Y. Singh, P. Gegenwart, K. R. Choi, S.-W. Cheong, P. J. Baker, C. Stock, and J. Taylor, Spin Waves and Revised Crystal Structure of Honeycomb Iridate Na_2IrO_3, Phys. Rev. Lett. **108**, 127204 (2012).

[40] S. Nishimoto, V. M. Katukuri, V. Yushankhai, H. Stoll, U. K. Rößler, L. Hozoi, I. Rousochatzakis, and J. van den Brink, Strongly frustrated triangular spin lattice emerging from triplet dimer formation in honeycomb Li_2IrO_3, Nat. Commun. **7**, 10273 (2016).

[41] R. Yadav, N. A. Bogdanov, V. M. Katukuri, S. Nishimoto, J. van den Brink, and L. Hozoi, Kitaev exchange and field-induced quantum spin-liquid states in honeycomb α-$RuCl_3$, Sci. Rep. **6**, 37925 (2016).

[42] K. Kitagawa, T. Takayama, Y. Matsumoto, A. Kato, R. Takano, Y. Kishimoto, S. Bette, R. Dinnebier, G. Jackeli, and H. Takagi, A spin–orbital-entangled quantum liquid on a honeycomb lattice, Nature (London) **554**, 341 (2018).

[43] D. Wulferding, Y. Choi, S.-H. Do, C. H. Lee, P. Lemmens, C. Faugeras, Y. Gallais, and K.-Y. Choi, Magnon bound states versus anyonic majorana excitations in the Kitaev honeycomb magnet α-$RuCl_3$, Nat. Commun. **11**, 1603 (2020).

[44] Y. Kasahara, T. Ohnishi, Y. Mizukami, O. Tanaka, S. Ma, K. Sugii, N. Kurita, H. Tanaka, J. Nasu, Y. Motome, T. Shibauchi, and Y. Matsuda, Majorana quantization and half-integer thermal quantum Hall effect in a Kitaev spin liquid, Nature (London) **559**, 227 (2018).

[45] Y. Kasahara, K. Sugii, T. Ohnishi, M. Shimozawa, M. Yamashita, N. Kurita, H. Tanaka, J. Nasu, Y. Motome, T. Shibauchi, and Y. Matsuda, Unusual Thermal Hall Effect in a Kitaev Spin Liquid Candidate α-$RuCl_3$, Phys. Rev. Lett. **120**, 217205 (2018).

[46] R. Hentrich, M. Roslova, A. Isaeva, T. Doert, W. Brenig, B. Büchner, and C. Hess, Large thermal Hall effect in α-$RuCl_3$: Evidence for heat transport by Kitaev-Heisenberg paramagnons, Phys. Rev. B **99**, 085136 (2019).

[47] T. Yokoi, S. Ma, Y. Kasahara, S. Kasahara, T. Shibauchi, N. Kurita, H. Tanaka, J. Nasu, Y. Motome, C. Hickey, S. Trebst, and Y. Matsuda, Half-integer quantized anomalous thermal Hall effect in the Kitaev material α-$RuCl_3$, arXiv:2001.01899.

[48] Y. Vinkler-Aviv and A. Rosch, Approximately Quantized Thermal Hall Effect of Chiral Liquids Coupled to Phonons, Phys. Rev. X **8**, 031032 (2018).

[49] M. Ye, G. B. Halász, L. Savary, and L. Balents, Quantization of the Thermal Hall Conductivity at Small Hall Angles, Phys. Rev. Lett. **121**, 147201 (2018).

[50] Y. J. Yu, Y. Xu, K. J. Ran, J. M. Ni, Y. Y. Huang, J. H. Wang, J. S. Wen, and S. Y. Li, Ultralow-Temperature Thermal Conductivity of the Kitaev Honeycomb Magnet α-$RuCl_3$ Across the Field-Induced Phase Transition, Phys. Rev. Lett. **120**, 067202 (2018).

[51] R. Hentrich, A. U. B. Wolter, X. Zotos, W. Brenig, D. Nowak, A. Isaeva, T. Doert, A. Banerjee, P. Lampen-Kelley, D. G. Mandrus, S. E. Nagler, J. Sears, Y.-J. Kim, B. Büchner, and C.

Hess, Unusual Phonon Heat Transport in α-$RuCl_3$: Strong Spin-Phonon Scattering and Field-Induced Spin Gap, Phys. Rev. Lett. **120**, 117204 (2018).

[52] D. Hirobe, M. Sato, Y. Shiomi, H. Tanaka, and E. Saitoh, Magnetic thermal conductivity far above the Néel temperature in the Kitaev-magnet candidate α-$RuCl_3$, Phys. Rev. B **95**, 241112(R) (2017).

[53] I. A. Leahy, C. A. Pocs, P. E. Siegfried, D. Graf, S.-H. Do, K.-Y. Choi, B. Normand, and M. Lee, Anomalous Thermal Conductivity and Magnetic Torque Response in the Honeycomb Magnet α-$RuCl_3$, Phys. Rev. Lett. **118**, 187203 (2017).

[54] L.-M. Duan, E. Demler, and M. D. Lukin, Controlling Spin Exchange Interactions of Ultracold Atoms in Optical Lattices, Phys. Rev. Lett. **91**, 090402 (2003).

[55] M. Schreiber, S. S. Hodgman, P. Bordia, H. P. Lüschen, M. H. Fischer, R. Vosk, E. Altman, U. Schneider, and I. Bloch, Observation of many-body localization of interacting fermions in a quasirandom optical lattice, Science **349**, 842 (2015).

[56] L. Barbiero, C. Schweizer, M. Aidelsburger, E. Demler, N. Goldman, and F. Grusdt, Coupling ultracold matter to dynamical gauge fields in optical lattices: From flux attachment to $\mathbb{Z}_2$ lattice gauge theories, Sci. Adv. **5**, eaav7444 (2019).

[57] E. Economou, *Green's Functions in Quantum Physics*, Springer Series in Solid-State Sciences (Springer, Berlin, 2006).

[58] Q. Luo, S. Hu, J. Zhao, A. Metavitsiadis, S. Eggert, and X. Wang, Ground-state phase diagram of the frustrated spin-$\frac{1}{2}$ two-leg honeycomb ladder, Phys. Rev. B **97**, 214433 (2018).

[59] J. Yoshitake, J. Nasu, Y. Kato, and Y. Motome, Majorana-magnon crossover by a magnetic field in the Kitaev model: Continuous-time quantum Monte Carlo study, Phys. Rev. B **101**, 100408(R) (2020).

[60] N. D. Patel and N. Trivedi, Magnetic field-induced intermediate quantum spin liquid with a spinon fermi surface, Proc. Natl. Acad. Sci. U.S.A. **116**, 12199 (2019).

[61] J. Nasu, M. Udagawa, and Y. Motome, Vaporization of Kitaev Spin Liquids, Phys. Rev. Lett. **113**, 197205 (2014).

[62] J. Nasu, M. Udagawa, and Y. Motome, Thermal fractionalization of quantum spins in a Kitaev model: Temperature-linear specific heat and coherent transport of majorana fermions, Phys. Rev. B **92**, 115122 (2015).

[63] P. A. Mishchenko, Y. Kato, and Y. Motome, Finite-temperature phase transition to a Kitaev spin liquid phase on a hyperoctagon lattice: A large-scale quantum Monte Carlo study, Phys. Rev. B **96**, 125124 (2017).

[64] A. Metavitsiadis, A. Pidatella, and W. Brenig, Thermal transport in a two-dimensional $\mathbb{z}_2$ spin liquid, Phys. Rev. B **96**, 205121 (2017).

[65] S. Widmann, V. Tsurkan, D. A. Prishchenko, V. G. Mazurenko, A. A. Tsirlin, and A. Loidl, Thermodynamic evidence of fractionalized excitations in α-$RuCl_3$, Phys. Rev. B **99**, 094415 (2019).

[66] S. Mandal, S. Bhattacharjee, K. Sengupta, R. Shankar, and G. Baskaran, Confinement-deconfinement transition and spin correlations in a generalized Kitaev model, Phys. Rev. B **84**, 155121 (2011).

[67] Y.-Z. You, I. Kimchi, and A. Vishwanath, Doping a spin-orbit mott insulator: Topological superconductivity from the

Kitaev-Heisenberg model and possible application to (Na$_2$/Li$_2$)IrO$_3$, Phys. Rev. B **86**, 085145 (2012).

[68] Although $J_2 \sim O(0.01J)$ for H_F to be valid, here we treat it as a free parameter to be able to detect a possible delocalization due to the TRS term, for a wide range of J_2.

[69] H.-D. Chen and Z. Nussinov, Exact results of the Kitaev model on a hexagonal lattice: Spin states, string and brane correlators, and anyonic excitations, J. Phys. A: Math. Theor. **41**, 075001 (2008).

[70] Z. Nussinov and G. Ortiz, Bond algebras and exact solvability of hamiltonians: Spin $s = \frac{1}{2}$ multilayer systems, Phys. Rev. B **79**, 214440 (2009).

[71] S. Mandal, R. Shankar, and G. Baskaran, RVB gauge theory and the topological degeneracy in the Honeycomb Kitaev model, J. Phys. A: Math. Theor. **45**, 335304 (2012).

[72] F. Evers and A. D. Mirlin, Anderson transitions, Rev. Mod. Phys. **80**, 1355 (2008).

[73] We have also tested this for different concentrations of defects $\langle \eta^z \rangle \neq 0$ with the same outcome.

[74] The unit cell chosen here is a linear combination of the one shown in Fig. 1 with the last z-bond removed and the same one

only shifted by one-rung, see also Refs. [13,14]. We have also tested other choices, which give no qualitative difference but at most some quantitative discrepancies at high frequencies.

[75] X. Zotos, High Temperature Thermal Conductivity of Two-Leg Spin-1/2 Ladders, Phys. Rev. Lett. **92**, 067202 (2004).

[76] R. Steinigeweg, J. Herbrych, X. Zotos, and W. Brenig, Heat Conductivity of the Heisenberg Spin-1/2 Ladder: From Weak to Strong Breaking of Integrability, Phys. Rev. Lett. **116**, 017202 (2016).

[77] Even the tiny finite values can be shown that go to zero as $L \to \infty$ by using an averaging over gauge configurations which allows to reach much larger system sizes [13].

[78] R. Steinigeweg, J. Gemmer, and W. Brenig, Spin-Current Autocorrelations from Single Pure-State Propagation, Phys. Rev. Lett. **112**, 120601 (2014).

[79] J. Nasu, J. Yoshitake, and Y. Motome, Thermal Transport in the Kitaev Model, Phys. Rev. Lett. **119**, 127204 (2017).

[80] A. Pidatella, A. Metavitsiadis, and W. Brenig, Heat transport in the anisotropic Kitaev spin liquid, Phys. Rev. B **99**, 075141 (2019).

[81] G. D. Mahan, *Many Particle Physics*, 3rd ed. (Plenum, New York, 2000).